Optical Near-Field Electron Microscopy

Raphaël Marchand,[1,2] Radek Šachl,[3] Martin Kalbáč,[3] Martin Hof,[3] Rudolf Tromp,[4,5] Mariana Amaro,[3] Sense J. van der Molen,[5] and Thomas Juffmann[1,2,*]

[1] *University of Vienna, Faculty of Physics, VCQ, Vienna A-1090, Austria*

[2] *University of Vienna, Max Perutz Laboratories, Department of Structural and Computational Biology, Vienna A-1030, Austria*

[3] *J. Heyrovský Institute of Physical Chemistry of the Czech Academy of Sciences, Dolejškova 3, Prague 182 23, Czech Republic*

[4] *IBM T.J. Watson Research Center, 1101 Kitchawan Road, Yorktown Heights, New York 10598, USA*

[5] *Huygens-Kamerlingh Onnes Laboratory, Leiden Institute of Physics, Leiden University, Leiden, Netherlands*

(Received 19 March 2021; revised 8 April 2021; accepted 14 June 2021; published 6 July 2021)

The imaging of dynamical processes at interfaces and on the nanoscale is of great importance throughout science and technology. While light-optical imaging techniques often cannot provide the necessary spatial resolution, electron-optical techniques damage the specimen and cause dose-induced artifacts. Here, optical near-field electron microscopy (ONEM) is proposed, an imaging technique that combines noninvasive probing with light, with a high-spatial-resolution readout via electron optics. Close to the specimen, the optical near fields are converted into a spatially varying electron flux using a planar photocathode. The electron flux is imaged using low-energy electron microscopy, enabling label-free nanometric resolution without the need to scan a probe across the sample. The specimen is never exposed to damaging electrons.

DOI: 10.1103/PhysRevApplied.16.014008

I. INTRODUCTION

Interfaces are of utmost importance throughout science, technology, industry, biology, and medicine. The imaging of dynamical processes happening at interfaces can yield crucial information on the underlying processes, ranging from electroplating, through corrosion to protein dynamics in lipid bilayers. Despite great progress over recent decades, there is currently no microscopy technique that can image dynamics at interfaces with nanometric resolution, label free, damage free, and over extended periods:

Optical super-resolution microscopy [1–6] has shown remarkable results over the past two decades, offering a resolution in the single-digit nanometer range for selected applications (see, e.g., Refs. [7,8] and references therein). But, besides phototoxicity, fluorescence-based methods face a tradeoff between frame rate, accuracy, and observation time, due to the finite number of photons that can be collected per fluorophore. And while high labeling density can affect biological function [9], low labeling density can lead to severe statistical artifacts due to blinking and bleaching [10]. Label-free optical techniques [such as interferometric scattering microscopy (iSCAT) [11,12] or plasmonics-enhanced protein characterization [13]] enable the detection and weighing of proteins but their spatial resolution is diffraction limited. Resolution of this issue by decreasing the wavelength to the x-ray regime is not an option for dynamic single-molecule studies, as they are precluded by the tradeoff between the signal-to-noise ratio and damage [14].

Scanning probe techniques enable atomic resolution in surface imaging [15] and subnanometer resolution in the imaging of membrane-bound proteins [16] but can perturb soft membranes in high-speed imaging [17]. Also, the scanning of the probe can limit imaging frame rates and the field of view. Similar tradeoffs are faced in near-field scanning optical microscopes, where, additionally, the finite probe size often limits the spatial resolution to tens of nanometers [18].

Electron optical techniques enable the determination of the ensemble-averaged atomic structure of proteins [19] and the imaging of the proteome of a cell [20]. However, these techniques require frozen samples, which precludes real-time imaging of dynamics. Recently, thin liquid cells have enabled the observation of proteins in their native environment within electron microscopes with nanometer resolution [21]. However, dose-induced damage leads to artifacts in electrochemical studies and limits extended dynamical studies of sensitive materials [22]. Recently, transmission electron microscopy at electronvolt energies (eV-TEM) has been developed by some of us [23], to

*thomas.juffmann@univie.ac.at

 © 2021 American Physical Society

decrease electron-induced damage while imaging. In fact, eV-TEM has been combined with low-energy electron microscopy (LEEM) so as to image samples in electron transmission and reflection at energies of $0 - 100$ eV [23]. Although the first results of the combination of these techniques are promising, this method is yet to prove itself for dynamical processes.

Techniques that correlate light and electron microscopy are promising alternatives to the techniques discussed above [24]. Traditionally, light microscopy is first used for live imaging, or for imaging with fluorescence-enabled specificity, and electron microscopy is then used to retrieve one final high-resolution snapshot of the specimen under study.

Here, we propose a technique that combines noninvasive probing with light with a readout based on electron optics offering nanometric resolution. Probing and readout are coupled via a photocathode placed in the optical near field of the scattered light, where the resolution is not limited by the optical wavelength. We will first describe the idea in more detail, then discuss its technological feasibility, its theoretical resolution and contrast, and lastly explore the potential application space of optical near-field electron microscopy (ONEM).

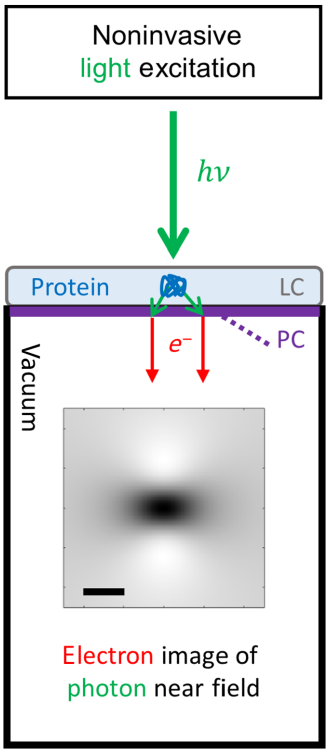

FIG. 1. Optical near-field electron microscopy (ONEM). Visible light illuminates a specimen (e.g., protein) in a liquid cell (LC). The resulting optical near-field interference pattern is converted into a spatially varying electron flux via a photocathode (PC). The spatial information is retrieved using aberration-corrected electron microscopy. Scale bar 5 nm.

II. CONCEPT

The proposed method is sketched in Fig. 1: Visible light is focused onto a sample (e.g., a protein) that is close to an ultrathin vacuum-liquid interface [e.g., in a liquid cell (LC) [25,26]]. The sample scatters light elastically, leading to nanometric features in the near field. This spatial light distribution is then converted, still in the near field, into a spatially varying electron flux via the photoelectric effect within a thin layer of low-work-function photocathode (PC) material [27,28]. The emitted photoelectrons are then imaged using aberration-corrected low-energy electron optics [29,30]. The electrons therefore provide a nondestructive readout of the nanometric optical near fields.

The proposed technique would be intrinsically damage free. First, low-work-function photocathodes can be efficiently excited with green light [27] and thus at photon energies significantly below the absorption band of most proteins. The inset in Fig. 1 shows the simulated near-field intensity distribution caused by a 50-kDa protein in water and at distance of 5 nm from the photocathode. Near-field simulations predict a signal-to-background ratio of about 1.4% (Fig. 1, simulated using the MNPBEM toolbox [31]). Shot-noise-limited detection, in which the intensity variance is proportional to the background, therefore requires about 5×10^3 photoelectrons per spatially resolved area to achieve a signal-to-noise ratio of 1. Assuming a photoelectron conversion efficiency of 3% (a conversion efficiency of approximately 15% has been measured for a 25–30-nm-thick photocathode [27] with excitation at 2.5 eV) and unity detection efficiency, this will require illuminating the protein with about 4.6×10^5 photons. For a frame rate of 1 kHz and 5 nm resolution, the required illumination intensity is about 2.5 μW μm^{-2}, i.e., well below intensities reported in, for example, iSCAT using light at 405 nm [11]. This is not surprising: both iSCAT and ONEM are shot noise limited. While iSCAT detects scattered light more efficiently (no photocathode), this is by far compensated by the narrower point spread function in ONEM, which increases contrast and resolution.

Second, the photocathode material will have a work function much lower than that of its liquid-cell support (1.9 eV for bialkali antimonide K_2CsSb [27], 1.3 eV for cesiated graphene [28], versus 4.4 eV for a few-layer graphene support [32]). The photocathode will be excited with visible light (e.g., $h\nu = 2.3$ eV for $\lambda = 532$ nm, where h is Planck's constant, ν is the frequency of the excitation light, and λ is its wavelength in vacuum), such that the energy of the created photoelectrons will be insufficient to overcome the internal potential barrier. The sample is therefore not exposed to electrons.

III. FEASIBILITY

The feasibility of ONEM relies on three technologies that have recently been developed independently.

First, electrons emitted from the photocathode have to be imaged with nanometer resolution. Interestingly, similar requirements are to be met in LEEM [29,30] and eV-TEM [23]. Typical LEEM systems have a lateral resolution of about 5 nm. In the past decade, however, aberration-corrected low-energy electron microscopy (AC LEEM) has been introduced, with an optimal resolution down to 1.5 nm and a field of view up to 75 μm [29,30]. Moreover, using novel algorithms, many images can now be stitched together smoothly. Thus, the effective field of view can be dramatically extended, without loss of resolution [33]. Furthermore, we note that a resolution smaller than 3 nm has been predicted for photoelectron emission microscopy (PEEM) on such state-of-the-art systems [29]. Figure 2 shows how ONEM can be implemented within an existing LEEM setup. The LEEM sample holder will be modified to allow for optical rear illumination of the sample. The low-work-function photocathode faces the LEEM objective lens, which extracts the emitted photoelectrons in a strong electrostatic field of 100 kV cm^{-1}. The electrons are accelerated to the column potential of 15 keV, after which they follow the red solid path in Fig. 2, from the photocathode, via an electron mirror (for aberration correction) and electron lenses, to the camera. The use of miniature objectives [34] within the light illumination path would allow for a correlative readout using light optics (dashed green line), which could provide additional information (e.g., molecular specificity via fluorescent labeling).

Second, in order to reach suboptical-wavelength resolution, the distance of the object to the photocathode layer needs to be much shorter than the optical wavelength. Ultrathin highly efficient photocathodes [27,28] have just been developed and have been shown to be smooth on the nanometer scale [35]. Most importantly, these photocathodes are efficient at green light excitation. Since these photocathodes are not to be exposed to air, they have to be prepared *in situ*, e.g., via evaporation, sputter deposition, or pulsed-laser deposition [36] from a solid photocathode target [37]. Alternatively, alkali metals or other photocathode materials could be stabilized in between graphene layers [27,38], potentially allowing for an *ex situ* preparation of the required photocathode.

Third, the study of specimens in their natural environment seems incompatible with the vacuum requirements for electron optics and the operation of photocathodes. Recently, however, this has become possible by the use of ultrathin interfaces between vacuum and air or liquid environments [39,40]. The latter have been developed for liquid-cell TEM [25] and modalities for electrochemistry experiments, photoactivation of specimens, and *in situ* specimen mixing are now commercially available.

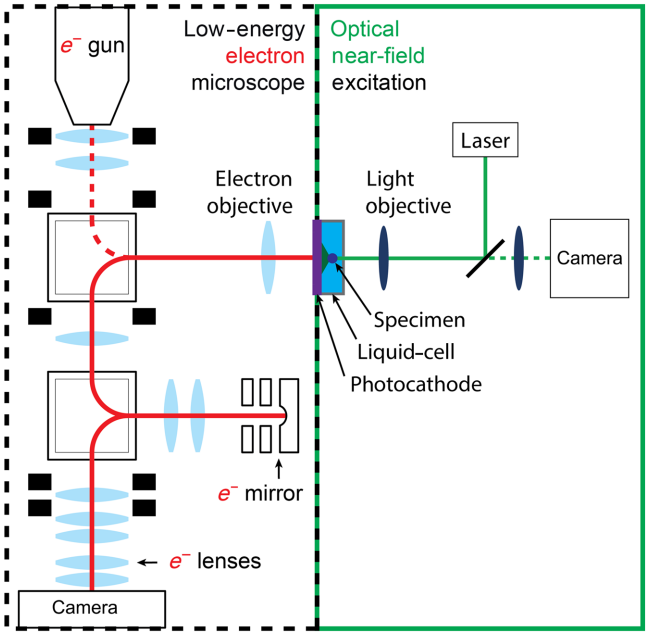

FIG. 2. A schematic of the ONEM setup. A specimen within a liquid cell is illuminated (solid green line) and optically inspected (dashed green line) with a continuous-wave (cw) laser. Photoelectrons (solid red line) generated in the photocathode at the backside of the liquid cell are imaged in an aberration-corrected LEEM. For this, the electrons travel through a set of lenses and are reflected by an aberration-correcting mirror. The electron gun at the top is off in ONEM but it can be turned on to perform LEEM experiments, e.g., on the photocathode material (dashed red line).

This toolbox can be directly applied for ONEM. Note that ONEM liquid cells do not need to be ultrathin, as it is light (and not electrons) that passes through the liquid, potentially allowing for more elaborate and robust sample manipulation.

The advance of the three techniques described above makes ONEM technologically feasible, allowing for damage-free measurements on dynamic processes in a liquid. Next, we discuss the contrast and resolution that ONEM could deliver.

IV. CONTRAST AND RESOLUTION

In the following section, we simulate the expected contrast and resolution of ONEM. All simulations are calculated using the MNPBEM toolbox [31]. We assume that the sample is excited with an x-polarized plane wave traveling in the z direction (reference field):

$$\vec{\mathbf{E}}_{\mathbf{ref}}(\vec{\mathbf{r}},t) = E_{\mathrm{ref}} e^{i(kz-\omega t)} \vec{\mathbf{u}}_{\mathbf{x}}, \tag{1}$$

where $k = 2\pi n_m \lambda^{-1}$, with $\lambda = 532$ nm the wavelength of the reference field in vacuum, ω its angular frequency, $n_m = 1.33$ the refractive index of water, and $\vec{\mathbf{u}}_{\mathbf{x}}$ a unitary

vector in the x direction. The particle of interest (e.g., protein, gold nanoparticle, copper cluster, etc.) is assumed to be spherical, with its center at the origin of the coordinate system [Fig. 3(a)]. The intensity distribution $I(\vec{\mathbf{r}})$ results from interfering the scattered field $\vec{\mathbf{E}}_{\mathbf{scat}}(\vec{\mathbf{r}},t)$ with the reference field $\vec{\mathbf{E}}_{\mathbf{ref}}(\vec{\mathbf{r}},t)$:

$$I(\vec{\mathbf{r}}) \propto ||\vec{\mathbf{E}}_{\mathbf{tot}}(\vec{\mathbf{r}},t)||^2 = ||\vec{\mathbf{E}}_{\mathbf{ref}}(\vec{\mathbf{r}},t) + \vec{\mathbf{E}}_{\mathbf{scat}}(\vec{\mathbf{r}},t)||^2. \quad (2)$$

Figures 3(b)–3(d) show the intensity distribution obtained for a protein in water (radius $R = 2.5$ nm, index of refraction $n_p = 1.44$) at a distance of $z = 5$ nm, $z = 50$ nm, and $z = 5$ μm, respectively.

On the z axis ($y = x = 0$), we observe the following behavior. In the near-field region ($R < z \ll \lambda$), [Fig. 3(b)], the scattered field is out of phase with the reference field, resulting in a total on-axis intensity, $I(0,0,z)$, smaller than the intensity of the reference field alone $I_0 \propto E_{\mathrm{ref}}^2$. In the far field ($\lambda \ll z$), [Fig. 3(d)], the scattered field is in phase with the reference field, leading to $I(0,0,z) > I_0$.

These results can be understood considering the model of an ideal radiating dipole, excited by the reference field. In this case, the total dipole moment of the particle is given by

$$\vec{\mathbf{p}}(t) = \epsilon_m \alpha \vec{\mathbf{E}}_{\mathbf{ref}}(\vec{\mathbf{0}},t), \quad (3)$$

where ϵ_m is the permittivity of the surrounding medium and α is the complex polarizability of the particle, given by

$$\alpha = 3V\frac{\epsilon_1 - \epsilon_m}{\epsilon_1 + 2\epsilon_m}, \quad (4)$$

where V is the volume of the particle and ϵ_1 the complex permittivity of the particle (see, e.g., ch. 5.2 in Ref. [41]). For a protein in water, α, ϵ_1, and ϵ_m are real and the dipole moment is in phase with the excitation field, which is consistent with the model of a Lorentz oscillator driven at frequencies far below the (material-dependent) resonance frequency (ch. 3.5 in Ref. [42]). The on-axis ($x = 0, y = 0$) scattered field is given by

$$\vec{\mathbf{E}}_{\mathbf{scat}}(0,0,z,t) = \frac{p(t)e^{i(kz-\omega t)}}{4\pi\epsilon_m}\left(\frac{k^2}{z} + \frac{ik}{z^2} - \frac{1}{z^3}\right)\vec{\mathbf{u}}_{\mathbf{x}}, \quad (5)$$

(ch. 9.2 in Ref. [43]). We find that the results of the simulations agree with the analytical expression to better than 2% (see Fig. S1 in the Supplemental Material [44]). For $z \ll 1/k$, the $-1/z^3$ term dominates and the scattered field is antiparallel to the reference field. For $1/k \ll z$, the $1/z$ term dominates and the scattered field is parallel to the reference field, in agreement with Figs. 3(b)–3(d). For $\lambda = 532$ nm and $n_m = 1.33$, the transition occurs at $z = 1/k \approx 64$ nm (see Fig. S2 in the Supplemental Material [44]).

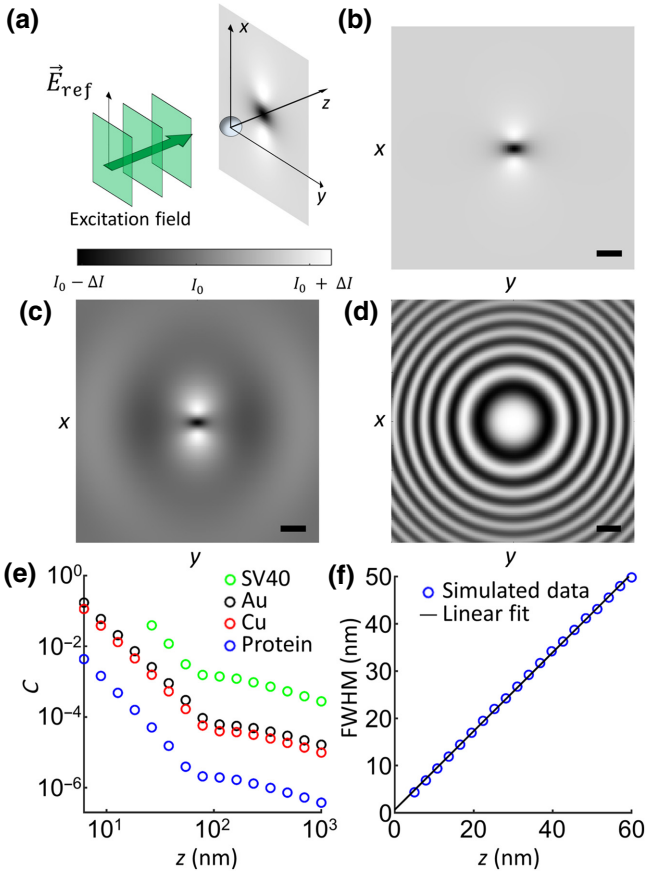

FIG. 3. (a) A three-dimensional drawing of a spherical nanoparticle and the interference pattern $I(x,y)$ obtained on a screen (photocathode) in the near field ($z = 5$ nm). (b)–(d) The simulated interference pattern $I(x,y)$ for a spherical protein of radius $R = 2.5$ nm and an index of refraction $n_p = 1.44$, at (b) $z = 5$ nm (scale bar 10 nm, $\Delta I/I_0 = 8 \times 10^{-3}$), (c) $z = 50$ nm (scale bar 100 nm, $\Delta I/I_0 = 6 \times 10^{-6}$), and (d) $z = 5$ μm (scale bar 1 μm, $\Delta I/I_0 = 8 \times 10^{-8}$). (e) The simulated Michelson contrast $C = (I_{\mathrm{max}} - I_{\mathrm{min}})(I_{\mathrm{max}} + I_{\mathrm{min}})^{-1}$ of the interference pattern $I(x,y)$ as a function of the distance of the screen, for gold (Au) particles, copper (Cu) particles, and proteins (all $R = 2.5$ nm), as well as for a simian virus 40 (SV40, $R = 22.5$ nm). (f) The full width at half maximum (FWHM) of the central feature of the simulated interference pattern $I(x,y)$ for a particle of radius $R = 2.5$ nm, as a function of the distance z to the particle (the FWHM is found to be independent of the particle material).

The simulated Michelson contrast

$$C = (I_{\mathrm{max}} - I_{\mathrm{min}})/(I_{\mathrm{max}} + I_{\mathrm{min}}), \quad (6)$$

as a function of the distance to the screen (i.e., the photocathode), is shown in Fig. 3(e) for different particle materials. The refractive indices of the protein and the virus are taken from Refs. [11] and [45], respectively. For gold (Au) and copper (Cu), the complex refractive indices are interpolated at 532 nm from data in Refs. [46] and [47], respectively. In the near field, the contrast is found to drop

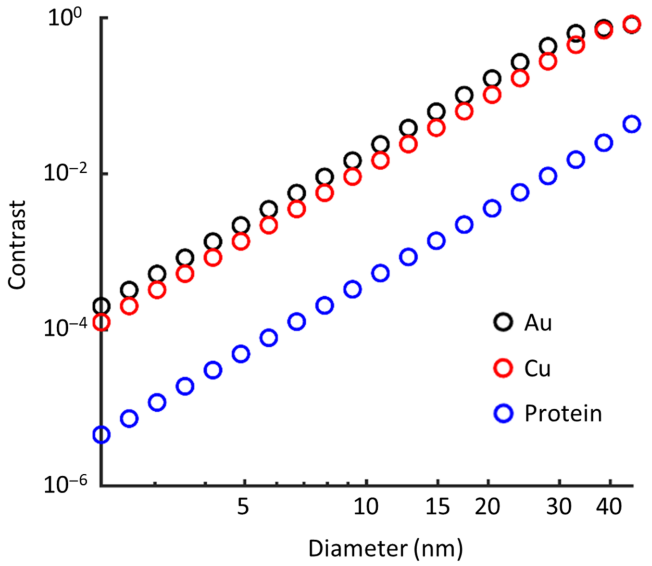

FIG. 4. The Michelson contrast of the simulated interference pattern $I(x, y)$ for a nanoparticle, as a function of the nanoparticle diameter, for $z = 25$ nm.

as $C \propto 1/z^3$, which will enable excellent suppression of signal from scatterers that are not bound to the interface. Figure 3(f) shows the resolution of ONEM as a function of z, evaluated by the full width at half maximum (FWHM) of the central feature in the interference pattern along the x direction. The calculation is again performed assuming a $R = 2.5$ nm protein. Within the plotted parameter range, the simulated FWHM increases linearly with the distance, with a fitted slope of $\partial \mathrm{FWHM}/\partial z = 0.82$.

The expected contrast as a function of the particle diameter is plotted in Fig. 4 for three different materials. All of them are assumed to be immersed in water and at a distance of 25 nm from the photocathode. In the absence of resonances, the polarizability is proportional to the volume of the particle, resulting in an R^3 dependence of the Michelson contrast. For metallic nanoparticles, the contrast is seen to saturate for particle radii > 20 nm.

V. POTENTIAL APPLICATION SPACE

By enabling dynamic studies of interfaces on the nanometer scale, ONEM has applications ranging from materials science to membrane biology.

One of these is the study of plasmonic fields. It is challenging to characterize light-matter interactions and devices based on optical near fields, on the nanometer scale. Laser-triggered electron microscopy has proven to be a versatile tool for mapping optical near fields on nanometer spatial and femtosecond temporal scales [48–50]. ONEM could enable this in liquid environments and at much lower optical excitation powers, allowing for a precise characterization, and consequent further development, of plasmonic (bio)sensors [13,51,52].

ONEM could also be applied in electrochemistry, studying, for example, the nucleation and growth of nanoscale copper clusters in a liquid environment. Such experiments have been the first application of *in situ* liquid-cell TEM [39], starting a new area of research that has grown rapidly over the past decade [25], both in material science and in biology. However, a serious and unresolved issue with such experiments is that the high-energy electron beam passes through the electrochemical cell above the working electrode, creating a large number of free solvated electrons. These can strongly affect the electrochemistry [22,53] and may even lead to the formation of hydrogen bubbles [54]. ONEM could be used to observe the nucleation and growth during electrodeposition with nanometer resolution and without electron-dose-induced artifacts. Successful implementation of this prototype liquid-cell experiment will open the door to the investigation of many electrochemical problems that are of significant industrial interest and that are currently out of reach for high-resolution real-time studies (e.g., corrosion, mass transport in batteries, swelling, liquid crystal switching, etc.).

Finally, ONEM could also be used to image proteins interacting on, in, or with biomembranes under conditions mimicking a native membrane environment. It has been shown that lipid bilayers can be formed on surfaces with the use of cushions or tethers to allow for the embedding of proteins in the membrane—in particular, transmembrane proteins—while maintaining the mobility and functionality of the inserted proteins [55–57]. If this is done on the vacuum-liquid interface, ONEM could be used for continuous high-resolution imaging (see Fig. S3 in the Supplemental Material [44] for simulated images of a circular array of spherical proteins in water). The first examples could include the visualization of supramolecular protein assemblies formed on lipid bilayers. In general, oligomerization of membrane proteins into multicomponent units is often critical for their function, or dysfunction. For instance, a change in the aggregation behavior of a proapoptotic protein Bax, the subsequent formation of Bax complexes with a broad distribution of oligomerization numbers, and, finally, the opening of functional pores in the mitochondrial membrane represent key steps in programmed cell death [58]. Similarly, supramolecular in-membrane assemblies consisting of 7–8 monomeric units are formed by a functionally unrelated protein named fibroblast growth factor 2 (FGF2), which regulates tumor growth and metastasis. ONEM has the potential to provide information on the dimensions [58–60] and also on the dynamics of these supramolecular complexes, the formation of which is crucial for cellular function. Additionally, since the contrast in ONEM decreases as $1/z^3$, unwanted protein signal from the solution is efficiently suppressed. It can therefore be used for imaging membrane related

processes even in the cases where the equilibrium between bound and unbound protein is shifted in favor of the unbound protein.

VI. DISCUSSION AND OUTLOOK

ONEM exploits light and electron optics according to their respective strengths: light for noninvasive probing and electrons for high-spatial-resolution readout. Light and electrons are coupled using an ultrathin photocathode and superresolution is enabled by the near-field components of the scattered light. ONEM is therefore ideally suited for the damage- and label-free study of physical, chemical, or biological processes happening at interfaces. A resolution below 5 nm and dynamic imaging over extended periods seem feasible. Various experimental difficulties will have to be overcome to realize such specifications. A low-energy electron microscope has to be modified to include a custom sample chamber and speckle-free optical excitation, as well as *in situ* photocathode coating capabilities. Coating procedures will have to be optimized for sensitivity and homogeneity and potential issues such as photocathode ageing, poisoning, or charging will have to be addressed.

ONEM can be operated, and extended, in many ways. Measurements can be performed in liquid, gas, or vacuum. They can be performed label free, characterizing the refractive-index distribution of a sample, or using labels (e.g., metal nanoparticles, fluorophores) bound to an object of interest. Correlative *in situ* light microscopy can provide additional information, for example, on the three-dimensional environment of the interface, optionally with fluorescence-enabled specificity. Polarization-dependent scattering cross sections (e.g., chiral molecules or chiral photonic structures) could enable shot-noise-limited measurements in challenging environments or in the presence of temporal changes of photocathode efficiency. Pump-probe measurements could make studies on ultrashort time scales possible.

ONEM offers unique measurement opportunities on the dynamics of various processes, by allowing for the use of liquid cells. Optical (plasmonic) properties of nanostructured materials can be probed in a liquid environment, which can yield information that is essential for bio-optical sensor design. Electrochemical experiments will yield insights into physical and chemical processes at interfaces, some of which play an important role in the energy transition. Finally, the exploration of tethered lipid bilayers will allow for the investigation of biological systems, offering information on protein clustering and dynamics within biological membranes.

Given recent developments in technology and methodology, we consider ONEM a feasible form of microscopy. Clearly, several practical challenges are still to be overcome, but once these are addressed, ONEM will offer opportunities for damage-free imaging of dynamic processes at interfaces.

ACKNOWLEDGMENTS

We thank Peter S. Neu for help with the figures. This project has received funding from the European Union's Horizon 2020 research and innovation program under Grant Agreement No. 101017902. T.J. acknowledges support from the European Research Council (ERC) "Microscopy—Making Optimal Use of Photons and Electrons" (MicroMOUPE) Grant No. 758752. R.M. acknowledges funding from the European Union's framework program for research and innovation, Horizon 2020 (2014–2020) under the Marie Curie Skłodowska Grant Agreement No. 847548. M.A. and M.H. acknowledge Czech Science Foundation (GAČR) Grant No. 19-26854X.

[1] S. W. Hell and J. Wichmann, Breaking the diffraction resolution limit by stimulated emission: Stimulated-emission-depletion fluorescence microscopy, Opt. Lett. **19**, 780 (1994).

[2] R. Heintzmann and T. Huser, Super-resolution structured illumination microscopy, Chem. Rev. **117**, 13890 (2017).

[3] M. J. Rust, M. Bates, and X. Zhuang, Sub-diffraction-limit imaging by stochastic optical reconstruction microscopy (STORM), Nat. Methods **3**, 793 (2006).

[4] E. Betzig, G. H. Patterson, R. Sougrat, O. W. Lindwasser, S. Olenych, J. S. Bonifacino, M. W. Davidson, J. Lippincott-Schwartz, and H. F. Hess, Imaging intracellular fluorescent proteins at nanometer resolution, Science **313**, 1642 (2006).

[5] T. Dertinger, R. Colyer, G. Iyer, S. Weiss, and J. Enderlein, Fast, background-free, 3D super-resolution optical fluctuation imaging (SOFI), Proc. Natl. Acad. Sci. **106**, 22287 (2009).

[6] N. Gustafsson, S. Culley, G. Ashdown, D. M. Owen, P. M. Pereira, and R. Henriques, Fast live-cell conventional fluorophore nanoscopy with ImageJ through super-resolution radial fluctuations, Nat. Commun. **7**, 1 (2016).

[7] Y. M. Sigal, R. Zhou, and X. Zhuang, Visualizing and discovering cellular structures with super-resolution microscopy, Science **361**, 880 (2018).

[8] S. J. Sahl, S. W. Hell, and S. Jakobs, Fluorescence nanoscopy in cell biology, Nat. Rev. Mol. Cell Biol. **18**, 685 (2017).

[9] E. A. Specht, E. Braselmann, and A. E. Palmer, A critical and comparative review of fluorescent tools for live-cell imaging, Annu. Rev. Physiol. **79**, 93 (2017).

[10] F. Baumgart, A. M. Arnold, B. K. Rossboth, M. Brameshuber, and G. J. Schütz, What we talk about when we talk about nanoclusters, Methods Appl. Fluoresc. **7**, 013001 (2018).

[11] M. Piliarik and V. Sandoghdar, Direct optical sensing of single unlabelled proteins and super-resolution imaging of their binding sites, Nat. Commun. **5**, 1 (2014).

[12] G. Young, *et al.*, Quantitative mass imaging of single biological macromolecules, Science **360**, 423 (2018).

[13] R. Gordon, Biosensing with nanoaperture optical tweezers, Opt. Laser Technol. **109**, 328 (2019).

[14] R. Henderson, The potential and limitations of neutrons, electrons and X-rays for atomic resolution microscopy of unstained biological molecules, Q. Rev. Biophys. **28**, 171 (1995).

[15] G. Binnig, H. Rohrer, C. Gerber, and E. Weibel, 7×7 Reconstruction on Si(111) Resolved in Real Space, Phys. Rev. Lett. **50**, 120 (1983).

[16] A. Engel and H. E. Gaub, Structure and mechanics of membrane proteins, Annu. Rev. Biochem. **77**, 127 (2008).

[17] T. Ando, High-speed atomic force microscopy and its future prospects, Biophys. Rev. **10**, 285 (2018).

[18] Y.-C. Yong, Y.-Z. Wang, and J.-J. Zhong, Nano-spectroscopic imaging of proteins with near-field scanning optical microscopy (NSOM), Curr. Opin. Biotechnol. **54**, 106 (2018), analytical Biotechnology.

[19] E. Nogales, The development of cryo-EM into a mainstream structural biology technique, Nat. Methods **13**, 24 (2016).

[20] J. Mahamid, S. Pfeffer, M. Schaffer, E. Villa, R. Danev, L. K. Cuellar, F. Förster, A. A. Hyman, J. M. Plitzko, and W. Baumeister, Visualizing the molecular sociology at the HeLa cell nuclear periphery, Science **351**, 969 (2016).

[21] U. M. Mirsaidov, H. Zheng, Y. Casana, and P. Matsudaira, Imaging protein structure in water at 2.7 nm resolution by transmission electron microscopy, Biophys. J. **102**, L15 (2012).

[22] T. J. Woehl, T. Moser, J. E. Evans, and F. M. Ross, Electron-beam-driven chemical processes during liquid phase transmission electron microscopy, MRS Bull. **45**, 746 (2020).

[23] D. Geelen, J. Jobst, E. Krasovskii, S. Van Der Molen, and R. Tromp, Nonuniversal Transverse Electron Mean Free Path through Few-Layer Graphene, Phys. Rev. Lett. **123**, 086802 (2019).

[24] A. Walter, P. Paul-Gilloteaux, B. Plochberger, L. Sefc, P. Verkade, J. G. Mannheim, P. Slezak, A. Unterhuber, M. Marchetti-Deschmann, M. Ogris, K. Bühler, D. Fixler, S. H. Geyer, W. J. Weninger, M. Glösmann, S. Handschuh, and T. Wanek, Correlated multimodal imaging in life sciences: Expanding the biomedical horizon, Front. Phys. **8**, 47 (2020).

[25] N. De Jonge and F. M. Ross, Electron microscopy of specimens in liquid, Nat. Nanotechnol. **6**, 695 (2011).

[26] M. Textor and N. de Jonge, Strategies for preparing graphene liquid cells for transmission electron microscopy, Nano Lett. **18**, 3313 (2018).

[27] H. Yamaguchi, F. Liu, J. DeFazio, M. Gaowei, C. W. Narvaez Villarrubia, J. Xie, J. Sinsheimer, D. Strom, V. Pavlenko, K. L. Jensen, *et al.*, Free-standing bialkali photocathodes using atomically thin substrates, Adv. Mater. Interfaces **5**, 1800249 (2018).

[28] H. Yuan, S. Chang, I. Bargatin, N. C. Wang, D. C. Riley, H. Wang, J. W. Schwede, J. Provine, E. Pop, Z.-X. Shen, *et al.*, Engineering ultra-low work function of graphene, Nano Lett. **15**, 6475 (2015).

[29] R. Tromp, J. Hannon, A. Ellis, W. Wan, A. Berghaus, and O. Schaff, A new aberration-corrected, energy-filtered LEEM/PEEM instrument. I. Principles and design, Ultramicroscopy **110**, 852 (2010).

[30] R. Tromp, J. Hannon, W. Wan, A. Berghaus, and O. Schaff, A new aberration-corrected, energy-filtered LEEM/PEEM instrument II. Operation and results, Ultramicroscopy **127**, 25 (2013).

[31] U. Hohenester and A. Trügler, MNPBEM—A MATLAB toolbox for the simulation of plasmonic nanoparticles, Comput. Phys. Commun. **183**, 370 (2012).

[32] N. Barrett, E. Conrad, K. Winkler, and B. Krömker, Dark field photoelectron emission microscopy of micron scale few layer graphene, Rev. Sci. Instrum. **83**, 083706 (2012).

[33] T. A. de Jong, D. N. Kok, A. J. van der Torren, H. Schopmans, R. M. Tromp, S. J. van der Molen, and J. Jobst, Quantitative analysis of spectroscopic low energy electron microscopy data: High-dynamic range imaging, drift correction and cluster analysis, Ultramicroscopy **213**, 112913 (2020).

[34] L. Yang, J. Wang, G. Tian, J. Yuan, Q. Liu, and L. Fu, Five-lens, easy-to-implement miniature objective for a fluorescence confocal microendoscope, Opt. Express **24**, 473 (2016).

[35] J. Feng, S. Karkare, J. Nasiatka, S. Schubert, J. Smedley, and H. Padmore, Near atomically smooth alkali antimonide photocathode thin films, J. Appl. Phys. **121**, 044904 (2017).

[36] D. Dijkkamp, T. Venkatesan, X. D. Wu, S. A. Shaheen, N. Jisrawi, Y. H. Min-Lee, W. L. McLean, and M. Croft, Preparation of Y-Ba-Cu oxide superconductor thin films using pulsed laser evaporation from high T_c bulk material, Appl. Phys. Lett. **51**, 619 (1987).

[37] M. Gaowei, Z. Ding, S. Schubert, H. B. Bhandari, J. Sinsheimer, J. Kuehn, V. V. Nagarkar, M. S. J. Marshall, J. Walsh, E. M. Muller, K. Attenkofer, H. J. Frisch, H. Padmore, and J. Smedley, Synthesis and x-ray characterization of sputtered bi-alkali antimonide photocathodes, APL Mater. **5**, 116104 (2017).

[38] M. Kalbác, L. Kavan, M. Zukalová, and L. Dunsch, Two positions of potassium in chemically doped C_{60} peapods: An *in situ* spectroelectrochemical study, J. Phys. Chem. B **108**, 6275 (2004).

[39] M. Williamson, R. Tromp, P. Vereecken, R. Hull, and F. Ross, Dynamic microscopy of nanoscale cluster growth at the solid-liquid interface, Nat. Mater. **2**, 532 (2003).

[40] Y. Han, K. X. Nguyen, Y. Ogawa, J. Park, and D. A. Muller, Atomically thin graphene windows that enable high contrast electron microscopy without a specimen vacuum chamber, Nano Lett. **16**, 7427 (2016).

[41] C. F. Bohren and D. R. Huffman, *Absorption and Scattering of Light by Small Particles* (Wiley, New York, 1998).

[42] E. Hecht, *Optics* (Pearson Education, London, 2017).

[43] J. D. Jackson, *Classical Electrodynamics* (Wiley, New York, 1998).

[44] See the Supplemental Material at http://link.aps.org/supplemental/10.1103/PhysRevApplied.16.014008 for a comparison between the analytical expression and numerical simulations, in the case of the on-axis scattered field; the interference pattern close to $z = 1/k$; and simulated images of a circular array of proteins in water.

[45] H. Ewers, V. Jacobsen, E. Klotzsch, A. E. Smith, A. Helenius, and V. Sandoghdar, Label-free optical detection and tracking of single virions bound to their receptors in supported membrane bilayers, Nano Lett. **7**, 2263 (2007).

[46] P. B. Johnson and R.-W. Christy, Optical constants of the noble metals, Phys. Rev. B **6**, 4370 (1972).

[47] E. D. Palik, *Handbook of Optical Constants of Solids II* (Academic Press, Orlando, 1998), Vol. 3.

[48] B. Barwick, D. J. Flannigan, and A. H. Zewail, Photon-induced near-field electron microscopy, Nature **462**, 902 (2009).

[49] L. Piazza, T. Lummen, E. Quinonez, Y. Murooka, B. Reed, B. Barwick, and F. Carbone, Simultaneous observation of the quantization and the interference pattern of a plasmonic near-field, Nat. Commun. **6**, 1 (2015).

[50] O. Kfir, H. Lourenço-Martins, G. Storeck, M. Sivis, T. R. Harvey, T. J. Kippenberg, A. Feist, and C. Ropers, Controlling free electrons with optical whispering-gallery modes, Nature **582**, 46 (2020).

[51] R. W. Taylor, R. J. Coulston, F. Biedermann, S. Mahajan, J. J. Baumberg, and O. A. Scherman, *In situ* SERS monitoring of photochemistry within a nanojunction reactor, Nano Lett. **13**, 5985 (2013).

[52] S.-H. Oh and H. Altug, Performance metrics and enabling technologies for nanoplasmonic biosensors, Nat. Commun. **9**, 1 (2018).

[53] T. J. Woehl, K. L. Jungjohann, J. E. Evans, I. Arslan, W. D. Ristenpart, and N. D. Browning, Experimental procedures to mitigate electron beam induced artifacts during *in situ* fluid imaging of nanomaterials, Ultramicroscopy **127**, 53 (2013).

[54] J. M. Grogan, N. M. Schneider, F. M. Ross, and H. H. Bau, Bubble and pattern formation in liquid induced by an electron beam, Nano Lett. **14**, 359 (2014).

[55] R. Macháň and M. Hof, Recent developments in fluorescence correlation spectroscopy for diffusion measurements in planar lipid membranes, Int. J. Mol. Sci. **11**, 427 (2010).

[56] F. Roder, S. Waichman, D. Paterok, R. Schubert, C. Richter, B. Liedberg, and J. Piehler, Reconstitution of membrane proteins into polymer-supported membranes for probing diffusion and interactions by single molecule techniques, Anal. Chem. **83**, 6792 (2011).

[57] K. R. Poudel, D. J. Keller, and J. A. Brozik, Single particle tracking reveals corralling of a transmembrane protein in a double-cushioned lipid bilayer assembly, Langmuir **27**, 320 (2011).

[58] Y. Subburaj, K. Cosentino, M. Axmann, E. Pedrueza-Villalmanzo, E. Hermann, S. Bleicken, J. Spatz, and A. J. García-Sáez, Bax monomers form dimer units in the membrane that further self-assemble into multiple oligomeric species, Nat. Commun. **6**, 1 (2015).

[59] J. P. Steringer, S. Lange, S. Čujová, R. Šachl, C. Poojari, F. Lolicato, O. Beutel, H.-M. Müller, S. Unger, Ü. Coskun, *et al.*, Key steps in unconventional secretion of fibroblast growth factor 2 reconstituted with purified components, Elife **6**, e28985 (2017).

[60] B. Antonsson, S. Montessuit, B. Sanchez, and J.-C. Martinou, Bax is present as a high molecular weight oligomer/complex in the mitochondrial membrane of apoptotic cells, J. Biol. Chem. **276**, 11615 (2001).